CRYSTAL GROWTH & DESIGN

Article

Cite This: Cryst. Growth Des. 2018, 18, 7633−7640

pubs.acs.org/crystal

Nanometer-Scale Residual Crystals in a Hot Melt Extruded Amorphous Solid Dispersion: Characterization by Transmission Electron Microscopy

Dana E. Moseson,[†,#] Naila A. Mugheirbi,[†,#] Andrew A. Stewart,[‡] and Lynne S. Taylor*[,†]

[†]Department of Industrial and Physical Pharmacy, College of Pharmacy, Purdue University, West Lafayette, Indiana 47907, United States

[‡]Department of Physics & Bernal Institute, University of Limerick, Limerick, Ireland

ABSTRACT: Common characterization techniques used to detect crystallinity in amorphous solid dispersions (ASD) typically have detection or quantification limits on the order of 1%. Herein, an amorphous solid dispersion of indomethacin and polyvinylpyrrolidone/vinyl acetate copolymer produced by hot melt extrusion was determined to be amorphous by powder X-ray diffraction and differential scanning calorimetry. However, through the use of transmission electron microscopy, residual crystals of two populations were identified: single crystals mid-dissolution (<100 nm) and nanocrystalline domains of 5−10 nm in size. Both domain types were observed to contain a high defect density. Polarized light microscopy and scanning electron microscopy techniques supplement these findings by corroborating crystallinity. The use of high resolution analytical techniques to identify and characterize residual crystallinity is considered an important first step to understand the significance of these residual crystalline populations to ASD performance attributes.

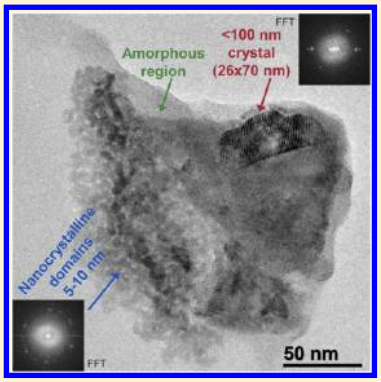

INTRODUCTION

Amorphous solid dispersions (ASDs) are an increasingly popular formulation strategy used to overcome poor aqueous solubility and slow dissolution of many drugs, improving bioavailability and therapeutic efficacy.[1,2] By crystalline-to-amorphous solid state transformation and subsequent stabilization by dispersion within an amorphous polymer, the solubility advantage of the amorphous form can often be realized.[3,4] Hot melt extrusion (HME) processes utilize thermal and mechanical input to form ASDs by melting and/or dissolving the drug into the molten polymer.[5] Given sufficient thermal input and mixing, a homogeneous molecular dispersion should result free of residual crystallinity.[6] However, if the transformation is incomplete, residual crystalline content may contribute to potential stability or dissolution performance issues.[7−9]

Powder X-ray diffraction (PXRD) is the gold standard technique for crystallinity detection and quantification in ASD formulations.[10] However, the technique is limited by mass fraction and dilution, crystal quality, as well as method parameters.[10−12] A complementary set of techniques would commonly be used to characterize a formulation, but have their own limitations which stem from properties of the instrument or sample. Polarized light microscopy (PLM) may be highly sensitive for detection of crystalline content, even when PXRD has determined a sample to be amorphous,[13] but this technique is limited by spatial resolution caused by the diffraction limitation. Differential scanning calorimetry (DSC) is limited by mass fraction, domain size, and the dynamic heating process.[6,14] Other studies have demonstrated that molecular-level differences in the amorphous phase can be identified by more sensitive techniques, such as Raman spectroscopy, even when PXRD and DSC have failed to identify these differences.[15,16]

The use of higher resolution analytical techniques may overcome some of these limitations in order to characterize residual crystalline content. Microscopy techniques such as transmission electron microscopy (TEM) have recently been found to be capable of detecting crystalline phases within ASDs.[17,18] Fast Fourier transform (FFT) analysis reveals periodic structure within TEM images, which may or may not be clearly visible in image space. The Fourier space image will produce sharp spots at frequencies corresponding to the lattice periodicities within the image, which in turn enables crystallinity to be confirmed and domains spatially identified within the micrograph. The inherent challenge of TEM is in preparing an electron-transparent sample on the order of 100 nm in thickness; however, the technique allows atomic distances to be visualized.[19,20]

Herein, an X-ray amorphous extrudate of a 1:1 blend of indomethacin (IDM) and polyvinylpyrrolidone/vinyl acetate copolymer (PVPVA) was prepared using HME processing conditions that correspond to the solubility temperature, i.e., the lowest temperature where a homogeneous molecular dispersion could theoretically be prepared.[6] Under these conditions, there is a significant risk of residual crystallinity if

Received: September 24, 2018
Revised: October 25, 2018
Published: October 26, 2018

DOI: 10.1021/acs.cgd.8b01435
Cryst. Growth Des. 2018, 18, 7633−7640

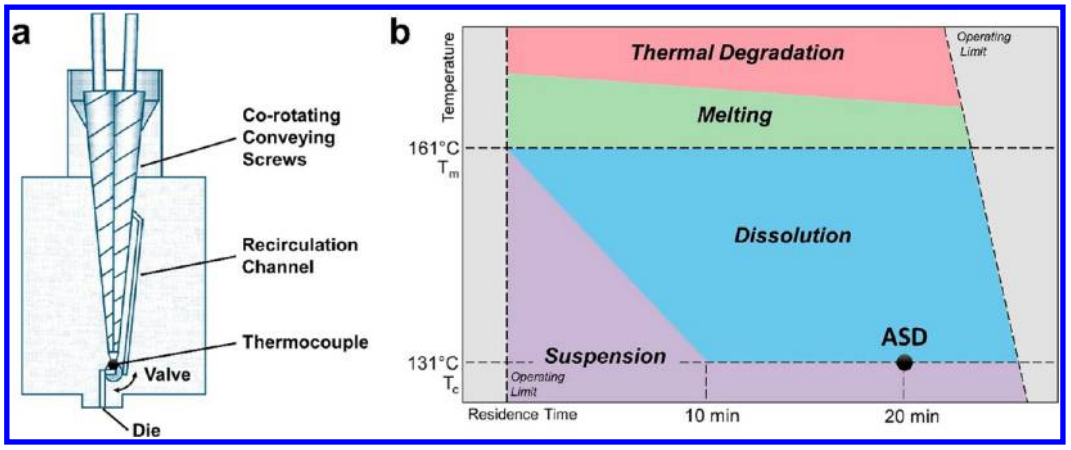

Figure 1. (a) Schematic of the hot melt extruder. (b) The process conditions of the IDM/PVPVA extrudate (ASD) are represented within a process operating space diagram, constructed based on the characterization of many samples found in our previous work.[6]

insufficient time or mixing conditions are provided. By processing for a long residence time to account for the kinetics of drug crystal dissolution, the extrudate was found to be amorphous by PXRD and DSC. However, through the use of high resolution characterization techniques, namely TEM, evidence of nanometer-scale crystallinity was found.

EXPERIMENTAL SECTION

Materials. Indomethacin (IDM, T_m = 161 °C) was obtained from ChemShuttle (Hayward, CA). Polyvinylpyrrolidone/vinyl acetate copolymer (PVPVA, Kollidon VA64, T_g = 104 °C) was a gift from BASF (Florham Park, NJ).

Methods. *Hot Melt Extrusion.* An Xplore Pharma melt extruder (Geleen, The Netherlands), assembled with the 5 mL corotating conveying screw and barrel set, was used at a screw speed of 20 rpm to prepare an extrudate of a 1:1 IDM/PVPVA premix (water corrected weight ratio). A schematic of the extruder used in this study is found in Figure 1a, and the temperature and time process conditions used are shown in the process operating design space diagram Figure 1b). A water bath set to 10 °C cooled the hopper, and the heating zone temperature was set to 134 °C, resulting in a bulk product melt temperature of 131 °C (as monitored by an in-line thermocouple located after the screw and prior to the recirculation channel or die). The recirculation valve was in the open position to extend the processing time; the valve was closed after 20 min to stop the recirculation and begin extruding the melt. The extrudate was allowed to cool at room temperature. A portion of the extrudate was cryomilled using a SPEX 6750 freezer/mill (Metuchen, NJ) for 60 s of grinding time at 10 Hz under liquid nitrogen to form a fine powder. Powders were then brought to room temperature and sieved to achieve particle size fractions of 100−250 μm and <100 μm. Extrudates and powders were stored in a refrigerator under desiccant until analysis.

Powder X-ray Diffraction (PXRD). Powder X-ray diffraction (PXRD) patterns were collected using a Rigaku SmartLab diffractometer (Rigaku Americas, The Woodlands, Texas) in Bragg−Brentano mode with a Cu−Kα radiation source and a d/tex ultra detector. Using a glass sample holder, the patterns of the extrudate powder (100−250 μm size fraction) were obtained from 5 to 40° 2θ, using a step size of 0.02° and a scan rate of 0.5° per min. The limits of detection and quantification were found to be 0.4% and 1%, respectively.[6]

Differential Scanning Calorimetry (DSC). A TA Q2000 differential scanning calorimeter equipped with a refrigerated cooling accessory (TA Instruments, New Castle, DE) purged with nitrogen at 50 mL/min was used to detect the T_g of the extrudate powder (<100 μm size fraction), as well as the constituent components. Each sample (3−5 mg, <100 μm size fraction) was loaded into a standard aluminum pan and heated from 0 to 180 °C at 5 °C/min with modulation of ±0.796 every minute, then cooled to 0 °C at 10 °C/min, followed by a second heating ramp at 10 °C/min.

Polarized Light Microscopy (PLM). The 100−250 μm size fraction powder samples or indomethacin particles were loaded in mineral oil on a glass slide and visually observed for birefringence using a Nikon Eclipse E600 POL cross-polarized light microscope (20× objective) with Nikon DS-Ri2 camera (Melville, NY). At least five images were captured to characterize the sample.

Transmission Electron Microscopy (TEM). Small pieces of the extrudate or indomethacin particles were sprinkled on a 300 mesh carbon-coated copper TEM grids with 5−6 nm standard thickness (SPI supplies, West Chester, PA). Extrudate pieces were placed on the TEM grid by gently touching/wiping the interior of the vial lid, which contained particulates fragmented from the bulk extrudate rods, with the carbon-coated side of the grid.

Bright-field transmission electron micrographs were acquired in an FEI Tecnai G20 electron microscope (FEI, Hillsboro, Oregon, USA) equipped with a LaB6 source, X-max 80 mm^2 silicon drift detector (Oxford Instruments, Abingdon, Oxfordshire, UK), and operated at 200 keV, 100 μm aperture, and a spot size of 1 (drug crystal images) or 3 (extrudate images). At least three grid squares were analyzed to identify particles that were suitably electron transparent for imaging.

Fast Fourier transform (FFT) analysis was performed using the Gatan DigitalMicrograph 3.21 software suite (Pleasanton, CA). Fourier filtering was applied using a spot mask symmetric about the origin of the FFT image, which selects only the desired frequencies (in reciprocal space). By then performing an inverse FFT on the masked image, the filtered image is reconstructed (in real space), which reveals only the periodic content associated with the specific FFT spot pair. ImageJ 1.51 (National Institutes of Health, Bethesda, MD) was used to apply false color imaging.

Scanning Electron Microscopy (SEM). Indomethacin particles or a cross section of the extrudate were fixed on a SEM stub using double-sided carbon tape, sputter-coated with platinum target for 60 s and examined with a FEI Nova nanoSEM field emission scanning electron microscope (FEI Company, Hillsboro, Oregon) operating at a 5 kV accelerating voltage, ~5 mm working distance, and a spot size of 3. A high-resolution through-the-lens detector (TLD) and Everhart Thornley detector (ETD) were used to image the extrudate and indomethacin particles, respectively.

RESULTS AND DISCUSSION

Characterization of Indomethacin Crystals. The IDM starting material was primarily composed of plate-like particles (Figure 2a,b), which consist of single crystals coated with smaller crystals as observed by extinguishing birefringence during rotation under polarized light (Figure 2a). The crystal lattice planes seen by TEM (Figure 2c−e) show micro-

DOI: 10.1021/acs.cgd.8b01435
Cryst. Growth Des. 2018, 18, 7633−7640

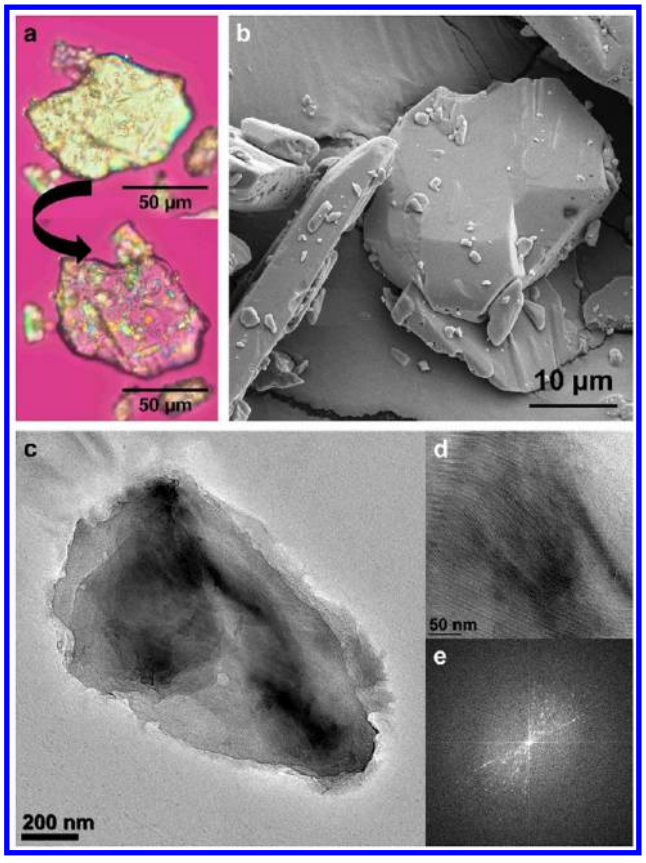

Figure 2. (a) Polarized light microscopy images of an IDM crystal, demonstrating extinguishing birefringence upon rotation. (b) Scanning electron microscopy (SEM) image of the IDM particles. (c) BF TE micrograph of an IDM particle. (d, e) BF TE micrograph of the crystalline microstructure and corresponding FFT pattern.

structure consistent with crystals in a variety of orientations, consistent with the observations from SEM and PLM, where small crystals are agglomerated or electrostatically affixed to the surface of larger crystals, and surface imperfections are evident.

Sample Preparation and Characterization. By applying high temperatures and mixing in an HME process, crystalline drug particles melt and/or dissolve into the molten polymer. On the basis of the temperature−composition phase diagram constructed previously,[6] processing conditions used to prepare the IDM/PVPVA extrudate were expected to generate a fully amorphous system. As shown in the process operating design space diagram (Figure 1b), within the dissolution regime, the crystalline drug can be fully solubilized at or above the formulation critical temperature T_c (131 °C), given sufficient mixing and residence time. Samples prepared at this lower bound of processing temperature have the greatest risk of residual crystalline content, if the solubility equilibrium is not satisfied, because drug crystal dissolution into a polymer melt is both a thermodynamically and kinetically driven process.

An ASD prepared at the formulation critical temperature T_c (131 °C) with 10 min of residence time was found to be X-ray amorphous, but had some birefringence detected using PLM. Hence, for TEM studies, the processing time was extended to 20 min. This extended processing time was selected to achieve complete dissolution of any residual crystals that may have been present after 10 min of processing time (below the PXRD limit of detection, 0.4%, but visible by PLM). Characterization by common analytical tools supported this supposition: no evidence of crystallinity is seen by PXRD (Figure 3a), a single

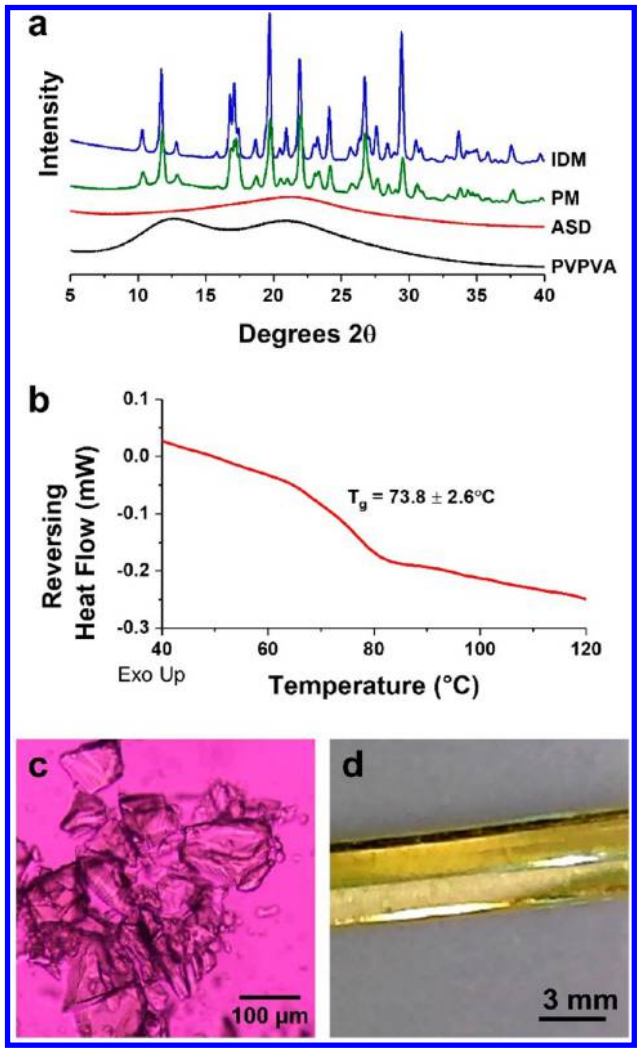

Figure 3. Characterization of the IDM/PVPVA extrudate (ASD). (a) X-ray powder diffraction patterns of PVPVA, ASD, physical mixture (PM), and pure IDM. The halo pattern of the ASD pattern indicates the sample is amorphous. (b) Reversing heat flow DSC thermogram of 1:1 IDM/PVPVA showing a single T_g. (c) Polarized light micrograph of 1:1 IDM/PVPVA. Trace birefringence is observed in some images. (d) The 1:1 IDM/PVPVA extrudate appears clear, indicating the sample is amorphous.

composite glass transition T_g is observed by DSC (Figure 3b), trace or no birefringence is seen by PLM (Figure 3c), and the extrudate is clear by visual assessment (Figure 3d).

Extrudate Characterization by Transmission Electron Microscopy. Multiple particles of the ASD extrudate were imaged using transmission electron microscopy (TEM), and both amorphous and crystalline domains were detected within (Figures 4, 5, and 6). Amorphous domains appear as a homogeneous continuous phase, while evidence of crystallinity includes darker areas within the matrix, diffraction contrast, and lattice planes.[17,18,21] Each of these particles shows broadly consistent, yet unique morphology. In particular, highly defective nanometer-scale crystallites of two populations are identified. First, discrete crystals (<100 nm) are observed mid-dissolution. Second, nanocrystalline domains of approximately

DOI: 10.1021/acs.cgd.8b01435
Cryst. Growth Des. 2018, 18, 7633−7640

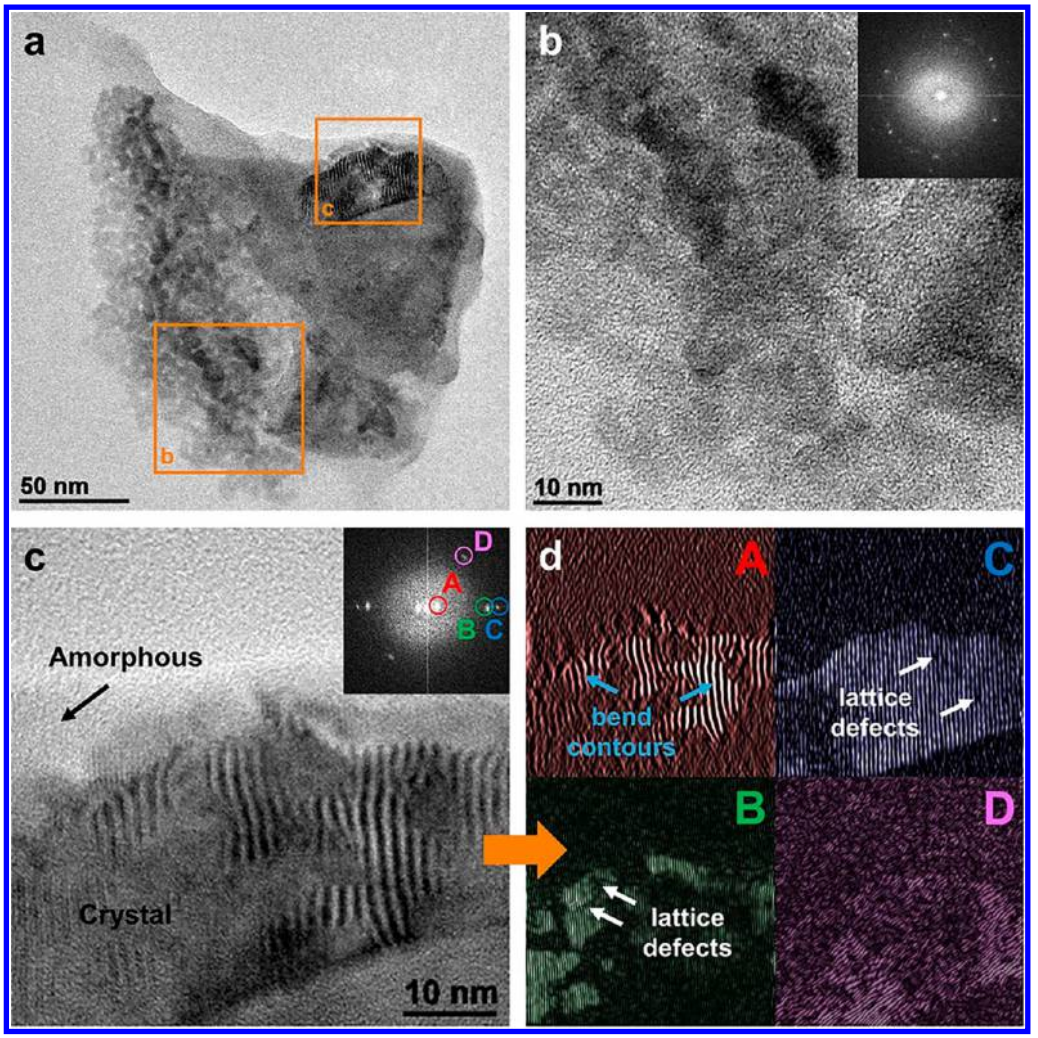

Figure 4. (a) BF TE micrograph of an ASD particle with residual crystallinity. (b) BF TE micrograph of the nanocrystalline domains and corresponding FFT pattern (inset). (c) BF TE micrograph of the ~26 × 70 nm discrete crystal and corresponding FFT pattern (inset). (d) Reconstructed BF TE micrographs from the inset of (c) generated using the inverse FFT function in the Gatan Suite. Each of the areas A–D is colorized to indicate the location where those patterns appear in the original image (c). Bend contours in A are highlighted by blue arrows; lattice defects, such as edge dislocations, are highlighted by white arrows.

5–10 nm in size, commonly in clusters, are observed. When observing small crystalline phases, it is often difficult to confirm the crystallinity by FFT, for a variety of reasons: the crystal orientation may have frequencies beyond those which can be recorded in the image, the specimen thickness may vary, causing some areas to be too thick to record a lattice image, the subsurface placement of the crystal within the particle obscures the lattice, the remaining degree of order in the domain, and the interference of the drug-polymer amorphous matrix.

The ASD particle shown in Figure 4a shows evidence of amorphous material and both populations of crystalline domains. The population of nanocrystalline domains is shown in Figure 4b. The FFT pattern (inset) confirms that many of the domains in this region are crystalline. The domains are clustered within the particle, suggesting that these domains originated from the same crystal and have not yet distributed and dissolved into the matrix. The domains in this image are 5.8 ± 1.2 nm in size (±SD, n = 20) and are randomly oriented, as demonstrated in the FFT. The random orientation, similarity of domain size, and clustering suggest a mechanical origin of these crystals.

A closer view of a discrete 26 × 70 nm crystal from this ASD particle is shown in Figure 4c, which clearly shows both amorphous and crystalline regions (confirmed by the FFT pattern inset). By applying an inverse FFT to each of these spots, the image can be reconstructed to show only the areas producing that order (Figure 4d: A–D). The lattice planes, now individually visualized, show dislocations and different degrees of thermally and/or mechanically induced structural deformation. The dark interference fringes seen in Figure 4d panel A are bend contours, which indicate curvature of the crystal arising due to strain at the interface of the crystal.[22,23] We hypothesize that this crystal, while defective, is still a single crystal. The reconstructed images Figure 4d, panels C and D are two lattice planes of the crystal and are found in almost the entire area of the crystal shape, while the planes found in Figure 4d, panels A and B (if superimposed) form a third, in-focus lattice plane.

Another ASD particle (Figure 5a) primarily contains areas that resemble crystalline domains, based on the appearance of the internal structure. A representative region is shown in Figure 5b. This partially crystalline area (also seen in the reconstructed false color images found in Figure 5c, panels A–

DOI: 10.1021/acs.cgd.8b01435
Cryst. Growth Des. 2018, 18, 7633–7640

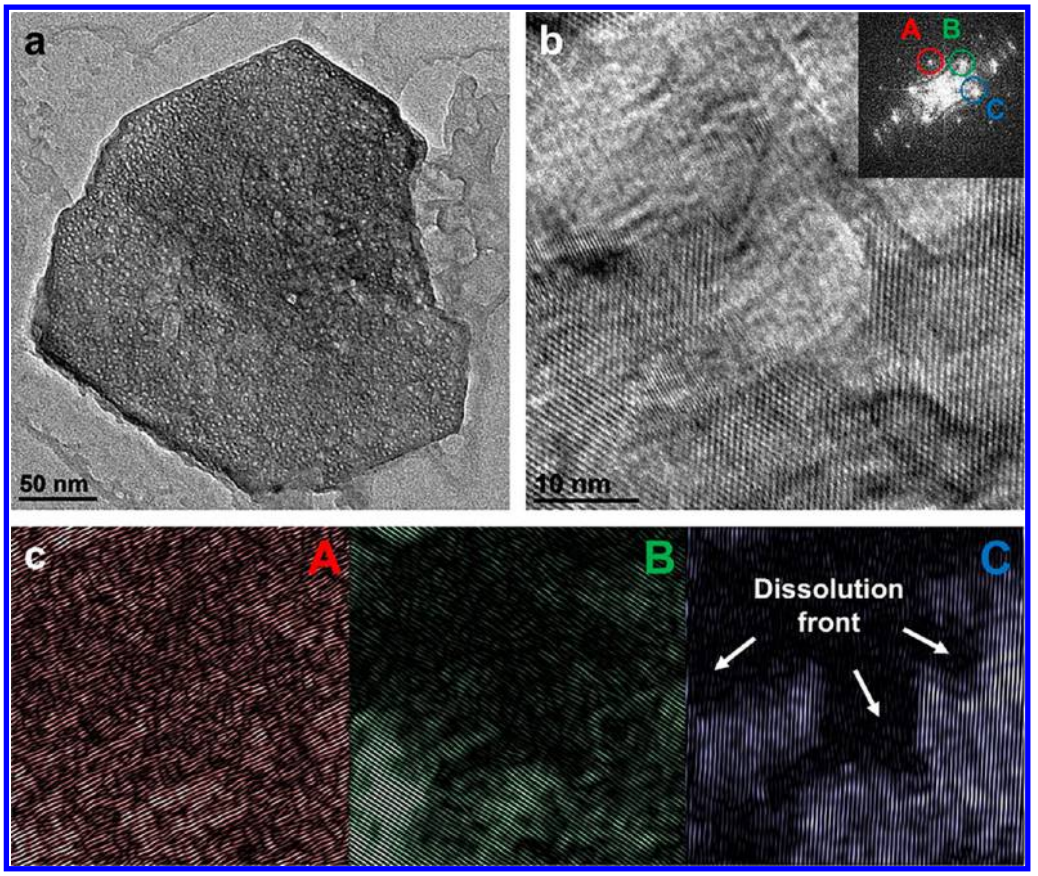

Figure 5. (a) TEM image of an ASD particle with residual crystallinity. (b) Representative region of the particle and corresponding FFT pattern (inset). (c) Inverse FFTs of areas A−C colorized to indicate the location where those patterns appear in the original image. The dissolution front is most apparent in C, highlighted by white arrows.

C) highlights a single lattice spacing in multiple orientations. This suggests that the crystal planes have been sheared with rotation in three distinct orientations. Each plane has a different level of dissolution, most clearly observed in Figure 5c, panel C.

The ASD particle shown in Figure 6a is also composed of amorphous and crystalline domains. Channels of amorphous material are observed, where polymer appears to have advanced into the crystalline regions. We hypothesize that the remaining crystalline domains in this particle may have originated from a discrete crystal, now segregated into smaller and partially dissolved domains. The appearance of the bend contours in Figure 6b is likely a result of crystal edges formed by dissolution of the crystal and strain at the interface with the amorphous matrix. Figure 6c shows a larger crystal with similar bend contours, which are highlighted in the false color reconstructions (Figure 6d).

Figure 6e contains both single crystals (orange circles) and nanocrystalline domains (yellow circles). The nanocrystalline domains in this region of the particle are more dispersed than those seen in Figure 4b, suggesting that, if also formed by the mechanical breakage mechanism, more time has elapsed since the event allowing the nanocrystals to further dissolve or distribute into the surrounding amorphous matrix. In the lower right of the Figure 6e, the orientation of the ∼60 nm crystal (also seen in the false color reconstructed image found in Figure 6f, panel B) highlights a single lattice spacing in multiple orientations, suggesting that the crystal planes have been sheared with rotation in multiple orientations. Bend contours are also seen on one edge of the crystal, suggesting strain and deformation at the interface (this crystal edge is also seen in the false color reconstructed image found in Figure 6f, panel C).

Extrudate Characterization by Scanning Electron Microscopy. The interior of the extrudate rod was imaged for evidence of crystallinity (Figure 7) using SEM. Some regions of the extrudate appear fully amorphous (Figure 7a), as no clear features appear on the surface. Some regions have embedded crystals in the size range of 10−1000 nm (Figure 7b, c). Due to the resolution capability of the instrument, domains smaller than 10 nm could not be imaged.

Comparison with Powder X-ray Diffraction. Ricarte et al. found that TEM was capable of detecting crystals in an X-ray amorphous physical mixture consisting of 3% crystalline drug,[17] while a much greater degree of sensitivity was found in this analysis. There are many underlying reasons for the sensitivity limitations of X-ray diffraction. Because of the dilution of drug by the polymer in an ASD, crystallinity detection becomes more challenging because of the resulting reduction in signal intensity associated with the crystalline peaks.[11,24] As crystallite size decreases, particularly into the nanometer range, peak broadening may limit detection of otherwise perfect crystals imbedded in an amorphous matrix.[25] Other sources of strain may influence peak detection, such as dislocations, stacking faults, and grain boundaries.[26] In the ASD sample characterized here, as well as many samples in our previous work and others in the literature,[6,27] crystalline

DOI: 10.1021/acs.cgd.8b01435
Cryst. Growth Des. 2018, 18, 7633−7640

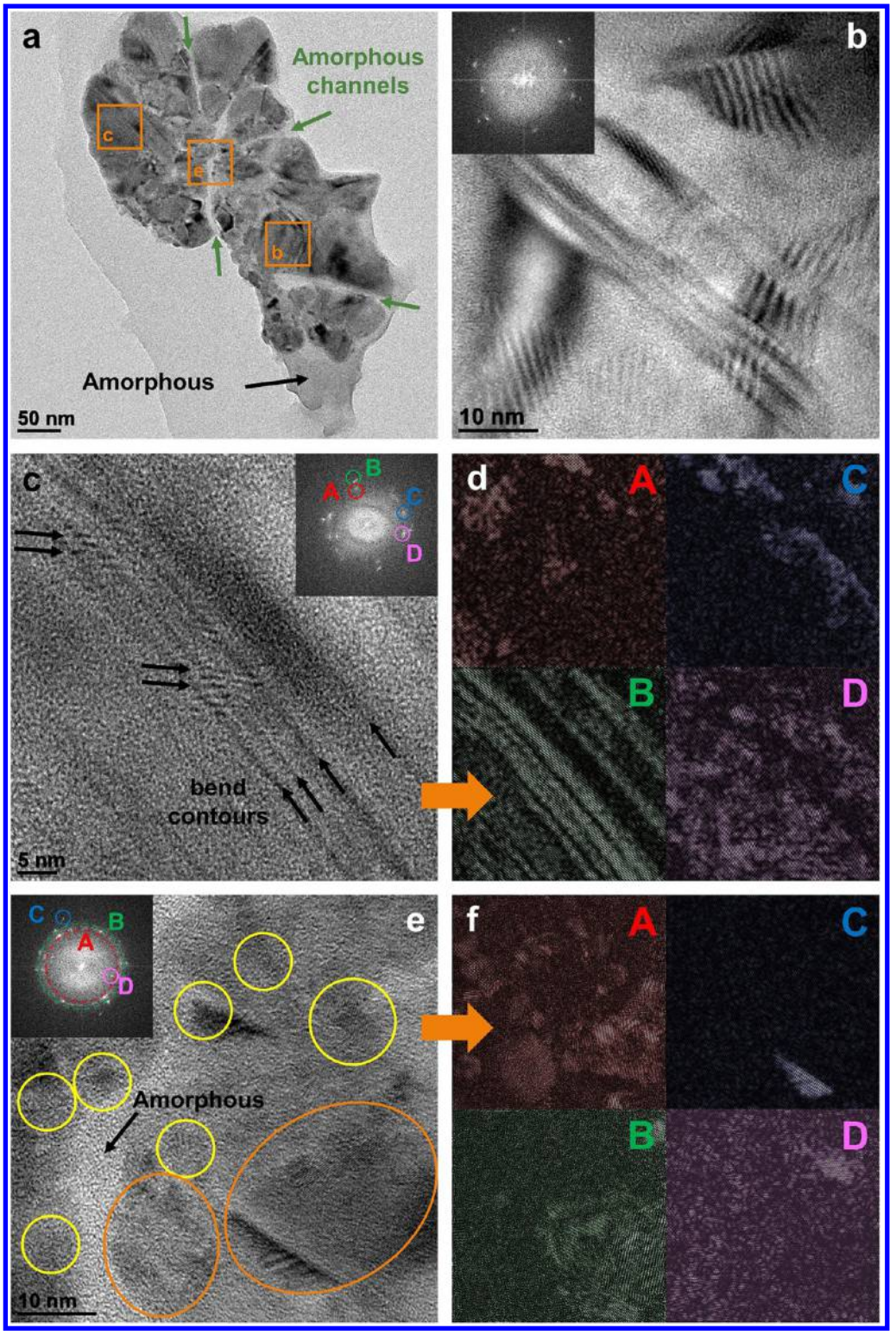

Figure 6. (a) BF TE micrograph of an ASD particle with residual crystallinity. Amorphous channels show areas of advancing polymer content. (b) Discrete crystal with bend contours and corresponding FFT pattern (inset). (c) BF TE micrograph of multiple crystals showing strain at the interface. (d) Reconstructed BF TE micrographs from the inset of (c) generated using the inverse FFT function in the Gatan Suite. Each of the areas A–D are colorized to indicate the location where those patterns appear in the original image (c). (e) BF TE micrograph showing multiple crystals and corresponding FFT pattern (inset). Domains in the 5–10 nm range are highlighted with yellow circles, and larger crystals are highlighted with orange circles. (f) Reconstructed BF TE micrographs from the inset of (e) generated using the inverse FFT function in the Gatan Suite. Each of the areas A–D is colorized to indicate the location where those patterns appear in the original image (e).

content, as quantified by PXRD, may be systematically underestimated based on these factors.

Crystal Dissolution Initiated from Defect Sites. As the starting material of drug crystals is likely to contain imperfections and local disorder at the surface and in the

DOI: 10.1021/acs.cgd.8b01435
Cryst. Growth Des. 2018, 18, 7633–7640

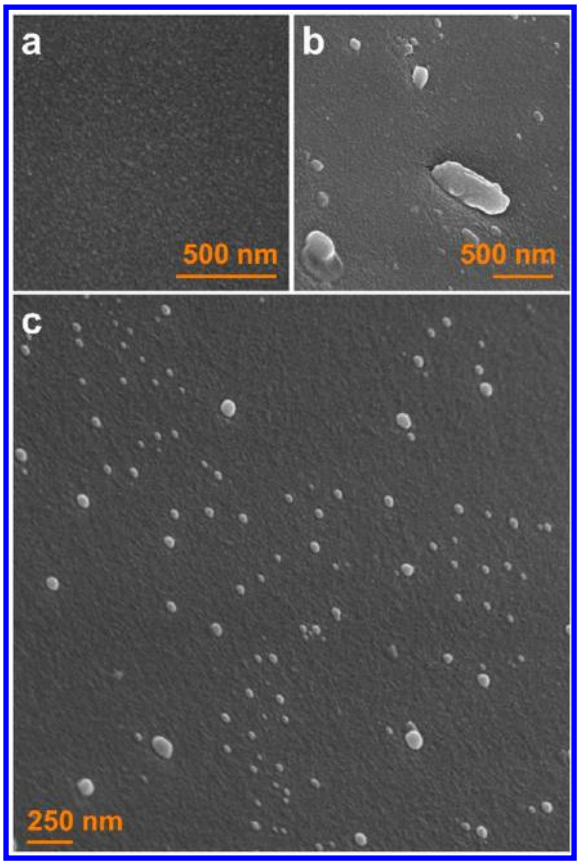

Figure 7. Scanning electron microscopy (SEM) images of the ASD extrudate. Some regions appear fully amorphous (a), or contain crystalline domains between 10 and 1000 nm (b, c). The length distribution of the domains found in (c) were measured as 38 ± 18 nm (±SD, n = 100).

bulk of the crystal,[28,29] these defects are the likely sites for initiation of phase transformation due to thermal or mechanical stresses because of higher overall free energy resulting from the presence of mixed amorphous and crystalline phases. Chemical and thermal etching studies have demonstrated that dissolution is initiated at defect sites[30,31] and that dissolution rate correlates to defect density.[32] Furthermore, contributions from the crystal structure, solvent−solid interactions, and the adsorption of the solvent molecule onto the crystal surface have been found to influence the dissolution mechanism at the crystal surface.[33,34] The highly defective nanocrystalline domains imaged in this extrudate suggest that defects, both those intrinsic to the crystals and those formed by mechanical damage, propagate as the crystals dissolve into the amorphous matrix, resulting in size reduction of crystals both through dissolution of external crystal surfaces as well as through fragmentation. Thus, due to HME processing under high temperature and shear, loss of crystallinity (i.e., increase in crystal defects) is expected, as an intermediate stage of the crystalline-to-amorphous transformation by mechanical damage and dissolution into the molten polymer.

CONCLUSIONS

Low levels of nanometer-scale residual crystals within a nominally amorphous drug−polymer dispersion prepared by hot melt extrusion were detected by TEM. This technique provided a high degree of sensitivity for the identification and microstructural characterization of two populations of nanocrystalline domains: single crystals <100 nm and clusters of 5−10 nm in size. The residual crystals show little similarity to the bulk crystalline starting material, as a result of thermally and/or mechanically induced structural deformation and dissolution into the amorphous matrix.

An open question remains whether or not any level, critical crystal size, or characteristic of residual crystals may be acceptable within ASDs, without causing detrimental physical stability or dissolution effects. The poor ability of common techniques to detect low levels of crystalline content contributes to the difficulty in addressing this question. The use of high resolution analytical techniques such as TEM to identify and characterize residual crystallinity is considered an important first step to understand the significance of these residual crystalline populations to ASD performance attributes.

AUTHOR INFORMATION

Corresponding Author

*E-mail: lstaylor@purdue.edu. Fax 765-494-6545. Phone 765-496-6614.

ORCID

Dana E. Moseson: 0000-0001-6986-8252

Lynne S. Taylor: 0000-0002-4568-6021

Author Contributions

#D.E.M. and N.A.M. contributed equally.

Notes

The authors declare no competing financial interest.

ACKNOWLEDGMENTS

The authors gratefully acknowledge financial support from the U.S. Food and Drug Administration (FDA) Grant Award 1U01FD005259-01, National Institute for Pharmaceutical Technology and Education Grant Award 5U01FD004275, and the Dane O. Kildsig Center for Pharmaceutical Processing Research. The Pharmaceutical Research and Manufacturers of America (PhRMA) Foundation is acknowledged for a postdoctoral fellowship granted to N.M. The National Science Foundation Graduate Research Fellowship program is acknowledged for financial support to D.M. under Grant Award DGE-1333468. Any opinions, findings, and conclusions or recommendations expressed in this material are those of the author(s) and do not necessarily reflect the views of the National Science Foundation. This article reflects the views of the authors and should not be construed to represent FDA's views or policies.

REFERENCES

(1) Van Den Mooter, G. The Use of Amorphous Solid Dispersions: A Formulation Strategy to Overcome Poor Solubility and Dissolution Rate. *Drug Discovery Today: Technol.* **2012**, *9*, e79.

(2) Jermain, S. V.; Brough, C.; Williams, R. O. Amorphous Solid Dispersions and Nanocrystal Technologies for Poorly Water-Soluble Drug Delivery − An Update. *Int. J. Pharm.* **2018**, *535*, 379−392.

(3) Murdande, S. B.; Pikal, M. J.; Shanker, R. M.; Bogner, R. H. Solubility Advantage of Amorphous Pharmaceuticals: I. A Thermodynamic Analysis. *J. Pharm. Sci.* **2010**, *99*, 1254−1264.

(4) Taylor, L. S.; Zhang, G. G. Z. Physical Chemistry of Supersaturated Solutions and Implications for Oral Absorption. *Adv. Drug Delivery Rev.* **2016**, *101*, 122−142.

(5) Crowley, M. M.; Zhang, F.; Repka, M. A.; Thumma, S.; Upadhye, S. B.; Kumar Battu, S.; McGinity, J. W.; Martin, C.

DOI: 10.1021/acs.cgd.8b01435
Cryst. Growth Des. 2018, 18, 7633−7640

Pharmaceutical Applications of Hot-Melt Extrusion: Part I. *Drug Dev. Ind. Pharm.* **2007**, *33*, 909−926.
(6) Moseson, D. E.; Taylor, L. S. The Application of Temperature-Composition Phase Diagrams for Hot Melt Extrusion Processing of Amorphous Solid Dispersions to Prevent Residual Crystallinity. *Int. J. Pharm.* **2018**, *533*, 454−466.
(7) Ivanisevic, I. Physical Stability Studies of Miscible Amorphous Solid Dispersions. *Int. J. Adv. Pharm.* **2018**, *99*, 4005−4012.
(8) Que, C.; Gao, Y.; Raina, S. A.; Zhang, G. G. Z.; Taylor, L. S. Paclitaxel Crystal Seeds with Different Intrinsic Properties and Their Impact on Dissolution of Paclitaxel-HPMCAS Amorphous Solid Dispersions. *Cryst. Growth Des.* **2018**, *18*, 1548−1559.
(9) Purohit, H. S.; Trasi, N. S.; Sun, D. D.; Chow, E. C. Y.; Wen, H.; Zhang, X.; Gao, Y.; Taylor, L. S. Investigating the Impact of Drug Crystallinity in Amorphous Tacrolimus Capsules on Pharmacokinetics and Bioequivalence Using Discriminatory In Vitro Dissolution Testing and Physiologically Based Pharmacokinetic Modeling and Simulation. *J. Pharm. Sci.* **2018**, *107*, 1330−1341.
(10) Shah, B.; Kakumanu, V. K.; Bansal, A. K. Analytical Techniques for Quantification of Amorphous/Crystalline Phases in Pharmaceutical Solids. *J. Pharm. Sci.* **2006**, *95*, 1641−1665.
(11) Rumondor, A. C. F.; Taylor, L. S. Application of Partial Least-Squares (PLS) Modeling in Quantifying Drug Crystallinity in Amorphous Solid Dispersions. *Int. J. Pharm.* **2010**, *398*, 155−160.
(12) Byrn, S. R.; Zografi, G.; Chen, X. S.. Solid-State Properties and Pharmaceutical Development. In *Solid State Properties of Pharmaceutical Materials*; John Wiley & Sons: Hoboken, NJ, 2017; pp 1−21.
(13) Haser, A.; Cao, T.; Lubach, J.; Listro, T.; Acquarulo, L.; Zhang, F. Melt Extrusion vs. Spray Drying: The Effect of Processing Methods on Crystalline Content of Naproxen-Povidone Formulations. *Eur. J. Pharm. Sci.* **2017**, *102*, 115−125.
(14) Sun, Y.; Tao, J.; Zhang, G. G. Z.; Yu, L. Solubilities of Crystalline Drugs in Polymers: An Improved Analytical Method and Comparison of Solubilities of Indomethacin and Nifedipine in PVP, PVP/VA, and PVAc. *J. Pharm. Sci.* **2010**, *99*, 4023−4031.
(15) Qian, F.; Huang, J.; Zhu, Q.; Haddadin, R.; Gawel, J.; Garmise, R.; Hussain, M. Is a Distinctive Single Tg a Reliable Indicator for the Homogeneity of Amorphous Solid Dispersion? *Int. J. Pharm.* **2010**, *395*, 232−235.
(16) Savolainen, M.; Heinz, A.; Strachan, C.; Gordon, K. C.; Yliruusi, J.; Rades, T.; Sandler, N. Screening for Differences in the Amorphous State of Indomethacin Using Multivariate Visualization. *Eur. J. Pharm. Sci.* **2007**, *30*, 113−123.
(17) Ricarte, R. G.; Lodge, T. P.; Hillmyer, M. A. Detection of Pharmaceutical Drug Crystallites in Solid Dispersions by Transmission Electron Microscopy. *Mol. Pharmaceutics* **2015**, *12*, 983−990.
(18) Mugheirbi, N. A.; Marsac, P. J.; Taylor, L. S. Insights into Water-Induced Phase Separation in Itraconazole-Hydroxypropylmethyl Cellulose Spin Coated and Spray Dried Dispersions. *Mol. Pharmaceutics* **2017**, *14*, 4387−4402.
(19) Thomas, J.; Gemming, T. *Analytical Transmission Electron Microscopy: An Introduction for Operators*; Springer: New York, 2014.
(20) Kolb, U.; Gorelik, T. E.; Mugnaioli, E.; Stewart, A. Structural Characterization of Organics Using Manual and Automated Electron Diffraction. *Polym. Rev.* **2010**, *50*, 385−409.
(21) Li, N.; Gilpin, C. J.; Taylor, L. S. Understanding the Impact of Water on the Miscibility and Microstructure of Amorphous Solid Dispersions: An AFM-LCR and TEM-EDX Study. *Mol. Pharmaceutics* **2017**, *14*, 1691−1705.
(22) Reimer, L.; Kohl, H. Imaging of Crystalline Specimens and Their Defects. In *Transmission Electron Microscopy: Physics of Image Formation*; Springer: New York, 2008; pp 359−418.
(23) Eddleston, M. D.; Jones, W. Observation and Characterization of Crystal Defects in Pharmaceutical Solids. In *Disordered Pharmaceutical Materials*; Wiley-VCH: Weinheim, Germany, 2016; pp 103−134.
(24) Rahman, Z.; Siddiqui, A.; Bykadi, S.; Khan, M. A. Determination of Tacrolimus Crystalline Fraction in the Commercial Immediate Release Amorphous Solid Dispersion Products by a Standardized X-Ray Powder Diffraction Method with Chemometrics. *Int. J. Pharm.* **2014**, *475*, 462−470.
(25) Langford, J. I.; Wilson, A. J. C. Scherrer after Sixty Years: A Survey and Some New Results in the Determination of Crystallite Size. *J. Appl. Crystallogr.* **1978**, *11*, 102−113.
(26) Ungar, T. Microstructure Parameters from X-Ray Line Profile Analysis. In *Advanced X-ray Techniques in Research and Industry*; IOS Press: Fairfax, VA, 2005; pp 268−286.
(27) Liu, H.; Wang, P.; Zhang, X.; Shen, F.; Gogos, C. G. Effects of Extrusion Process Parameters on the Dissolution Behavior of Indomethacin in Eudragit E PO Solid Dispersions. *Int. J. Pharm.* **2010**, *383*, 161−169.
(28) Jones, W.; Eddleston, M. D. Crystal Imperfections in Molecular Crystals: Physical and Chemical Consequences. In *Disordered Pharmaceutical Materials*; 2016; pp 85−102.
(29) Newman, A.; Zografi, G. Critical Considerations for the Qualitative and Quantitative Determination of Process-Induced Disorder in Crystalline Solids. *J. Pharm. Sci.* **2014**, *103*, 2595−2604.
(30) Keith, R. E.; Gilman, J. J. Dislocation Etch Pits and Plastic Deformation in Calcite. *Acta Metall.* **1960**, *8*, 1−10.
(31) Vasilchenko, M. A.; Shakhtshneider, T. P.; Boldyrev, V. V.; Naumov, D. Y. The Morphology of Etch Pits During Thermal Treatment of Drugs and Its Dependence on the Features of Their Crystallochemical Structure. *J. Therm. Anal.* **1999**, *57*, 157−164.
(32) Burt, H. M.; Mitchell, A. G. Crystal Defects and Dissolution. *Int. J. Pharm.* **1981**, *9*, 137−152.
(33) Wen, H.; Li, T.; Morris, K. R.; Park, K. Dissolution Study on Aspirin and α-Glycine Crystals. *J. Phys. Chem. B* **2004**, *108*, 11219−11227.
(34) Li, T. L.; Morris, K. R.; Park, K. Influence of Solvent and Crystalline Supramolecular Structure on the Formation of Etching Patterns on Acetaminophen Single Crystals: A Study with Atomic Force Microscopy and Computer Simulation. *J. Phys. Chem. B* **2000**, *104*, 2019−2032.

DOI: 10.1021/acs.cgd.8b01435
Cryst. Growth Des. 2018, 18, 7633−7640